Bound States in the Continuum in Cylindrical All-Dielectric Metasurface Cavities

Brugnolo, Pietro ; Arslanagic, Samel; Jacobsen, Rasmus E.

Published in:
Physical Review Letters

Link to article, DOI:
10.1103/PhysRevLett.134.096902

Publication date:
2025

Document Version
Peer reviewed version

Bound States in the Continuum in Cylindrical All-Dielectric Metasurface Cavities

Pietro Brugnolo, Samel Arslanagić and Rasmus E. Jacobsen
Department of Space Research and Technology,
Technical University of Denmark,
Lyngby DK-2800, Denmark
(Dated: November 29, 2024)

Bound states in the continuum are presently demonstrated in all-dielectric, metasurface-based cavities of circularly cylindrical shapes. While their cross-sectional sizes may be arbitrary, emphasis is put on the much-needed excitation of these intriguing states in sub-wavelength cavities. The employed metasurfaces are characterized by effective electric and magnetic surface impedances, allowing for a swift analytical analysis of the underlying problem. The inclusion of magnetic responses, in addition to the electric one, enhances the versatility of the proposed cavities, significantly extending their application, particularly in optical contexts where magnetism is absent. To demonstrate the potential of the proposed method, an all-dielectric metasurface composed of appropriately arranged silicon particles is designed and investigated in the optical frequency range, resulting in a quality factor of $\sim 1.7 \times 10^4$.

Bound states in the continuum (BICs) are highly resonant states localized in structures open to incoming waves [1–5]. Theoretically, BICs possess infinite quality factors (Q-factors), producing near field enhancements of non-decaying nature, making them interesting in terms of fundamental physics and for many industrial applications [6, 7]. They are found to occur when zeros and poles of a Hermitian system coincide [8]. Originally predicted in quantum systems [9], they have since then been observed in a range of wave settings, including acoustics [10], hydrodynamics [11] and electromagnetics [1]. Focusing on the latter case, they are typically observed in photonic (periodic) and plasmonic configurations, and in structures with extreme material parameters, such as epsilon-near-zero (ENZ) materials and perfect electric conductors [12–16]. For practical implementations, a reasonable coupling with external fields is necessary to excite the resonance, resulting in quasi-BICs. This is achieved by slightly detuning the system away from the ideal BIC condition. Including ineluctable structural irregularities and material losses, their Q-factors become finite.

BICs in arrays, such as metasurfaces (MSs), have mostly been studied in optics. This is because the Q-factor scales with the total number of array elements, essentially making them impractical for low-frequency applications. Low-loss dielectrics are the preferred material choice in optics due to severe metal losses at these frequencies. Several all-dielectric MSs have been investigated for various applications including lasing, sensing and wavefront manipulations [5, 17, 18]. Extreme Q-factors have been demonstrated in all-dielectric MSs [5], reaching values as high as $\sim 10^6$ [19]. However, the underlying (quasi-) BICs are in many cases spatially extended, often leading to a low local density of states [13]. At the same time, recent studies explored the use of the BIC theory in plasmonic structures [15, 20–24], culminating in a comprehensive strategy that, exploiting the balance of local and non-local responses of the MS, tailors the dissipative behaviour of the resonant modes attaining high Q-factors [24]. Furthermore, quasi-BICs in single metallic and dielectric resonators exhibit significant field localization with small modal volumes [16, 25–28].

The resonances found in regular cavities, such as Fabry-Pérot interferometers and metallic microwave cavities, are also highly localized states. However, such cavities are composed of highly reflecting surfaces making them inaccessible for external excitation. Recently, it was shown that reflecting MSs can form cavities supporting similar modes as the regular cavities [29–31], but allowing external excitation. At microwave frequencies, cylindrical and planar cavities formed by one and two MSs, respectively, have been investigated [30, 31]. Both geometries rely on MSs with effective surface impedances close to zero, resulting in quasi-perfect electric conductors. These resonant MSs have specific size requirements: in the planar case, the two MSs must be spaced by a multiple of $\lambda/2$, with λ being the wavelength, whereas for the cylindrical cavity, the resonance conditions are the roots of the cylindrical Bessel functions. In both the planar and cylindrical cases, the effective surface impedance of the MSs originate merely from electric dipole excitations, and thus no magnetic effects were considered. In addition, these MSs utilize substrates with metallic patterns and metallic particles at microwave and optical frequencies, respectively.

In this work, we demonstrate that BICs can be formed in cavities of any size by utilizing all-dielectric MSs with both electric and magnetic surface impedances. The magnetic response, on top of the electric one, expand the versatility of the proposed cavities and go beyond the application potential of electric-only configurations, specifically at optics where magnetic materials are absent. The theoretical foundation is presented together with the analytical solutions for the required electric and magnetic surface impedance. All-dielectric MS designs are subsequently explored for potential optical applications. The synthesized MSs consist of spherical dielectric particles, and their effective surface impedances are determined using the model reported in [32]. This enables an analytical approach, and we compare the analytical results for se-

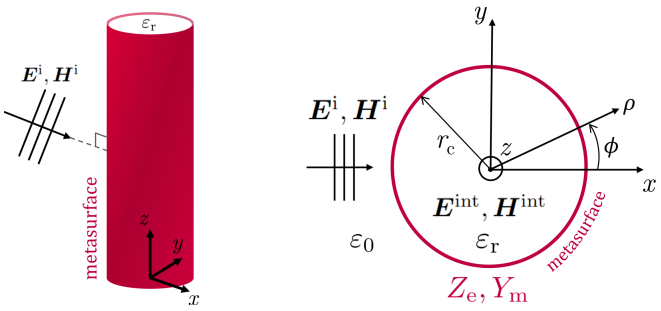

FIG. 1. Left: Sketch of the investigated cylindrical MS cavity illuminated by a plane wave. Right: cross-sectional view of the cavity. See the main text for a detailed explanation of the configuration.

lected MSs with the full-wave simulations confirming the existence of the quasi-BICs, with a Q-factor of $\sim 1.7\times10^4$ induced by the MS made of silicon particles. Throughout the work, the time factor $\exp(j\omega t)$, where ω is the angular frequency and t is the time, has been assumed and suppressed.

A 3D sketch of the configuration of interest (left) and its cross-section (right) are shown in Fig. 1. The configuration consists of an infinitely long cylindrical dielectric cavity of radius r_c and relative permittivity ε_r. The cavity is enclosed by a concentric cylindrical MS characterized by an electric surface impedance Z_e and a magnetic surface impedance Z_m, and is illuminated by a linearly polarized plane wave travelling in the $+x$ direction. Throughout this work, we employ the magnetic surface admittance $Y_m = 1/Z_m$. The axis of the cylinder coincides with the z-axis of the Cartesian coordinate system (x, y, z), associated with the cylindrical coordinate system (ρ, ϕ, z). Using the classical Lorenz-Mie analysis for cylindrical harmonics and considering a TE^z polarization, magnetic fields are given by [33]:

$$\begin{aligned}
\boldsymbol{H}^i &= \hat{\mathbf{z}} H_0 \sum_{n=-\infty}^{\infty} j^{-n} J_n(k_0\rho)\exp(jn\phi),\\
\boldsymbol{H}^s &= \hat{\mathbf{z}} H_0 \sum_{n=-\infty}^{\infty} A_n^{TE} H_n^{(2)}(k_0\rho)\exp(jn\phi),\\
\boldsymbol{H}^{int} &= \hat{\mathbf{z}} H_0 \sum_{n=-\infty}^{\infty} B_n^{TE} J_n(k_1\rho)\exp(jn\phi),
\end{aligned} \tag{1}$$

where H_0 is the magnitude, $k_0 = 2\pi/\lambda_0$ ($k_1 = k_0\sqrt{\varepsilon_r}$) is the host free-space (dielectric cavity) wavenumber, λ_0 is the free-space wavelength, $\boldsymbol{H}^i$, $\boldsymbol{H}^s$, and $\boldsymbol{H}^{int}$ are, respectively, the incident, scattered and internal magnetic fields and A_n^{TE} and B_n^{TE} are the expansion coefficients for the scattered and the internal field. $J_n(\cdot)$ and $H_n^{(2)}(\cdot)$ denote the n-th order Bessel functions of the first kind and Hankel functions of the second kind, respectively. In the absence of magnetoelectric effects, and assuming the MS to be infinitely thin, the analytical expressions for the expansion coefficients can be derived solving the boundary conditions on $\rho = r_c$ [34, 35]:

$$\begin{aligned}
\hat{\mathbf{n}}\times\left(\boldsymbol{E}^{int} - (\boldsymbol{E}^i + \boldsymbol{E}^s)\right) &= -\frac{\boldsymbol{H}^{int}_{tan} + \boldsymbol{H}^i_{tan} + \boldsymbol{H}^s_{tan}}{2Y_m},\\
\hat{\mathbf{n}}\times\left(\boldsymbol{H}^{int} - (\boldsymbol{H}^i + \boldsymbol{H}^s)\right) &= \frac{\boldsymbol{E}^{int}_{tan} + \boldsymbol{E}^i_{tan} + \boldsymbol{E}^s_{tan}}{2Z_e},
\end{aligned} \tag{2}$$

where $\hat{\mathbf{n}} = -\hat{\boldsymbol{\rho}}$ is the normal unit vector to the surface, $\boldsymbol{E}^i$, $\boldsymbol{E}^s$, and $\boldsymbol{E}^{int}$ are respectively the incident, scattered and internal electric fields and the subscript "tan" indicates the tangential components of the field to the surface. The analytical solutions to the coefficients are provided in the Supplementary Material. Analyzing the solutions for the internal coefficients, we notice that the condition $Z_eY_m = 1/4$ corresponds to a zero in the numerator of their expression. This implies that the field inside the cavity vanishes, as seen directly also from the boundary conditions in (2). It is straightforward to find solutions for Z_e and Y_m that identify the conditions required for BICs. These simply correspond to the crossing of zeros and poles of the internal coefficient B_n^{TE}. The required conditions are thus found by applying the condition $Z_eY_m = 1/4$, which gives the zeros of B_n^{TE}, while at the same time requiring its denominator to be zero in order to provide the poles of B_n^{TE}. For the TE^z polarization this corresponds to solving the following system of equations:

$$\begin{cases}
Z_eY_m = 1/4,\\
8\eta_0 H_n^{(2)\prime}(x_0)J_n(x_1) - 8\eta_1 H_n^{(2)}(x_0)J_n'(x_1)\\
+\frac{1}{j}\left(\frac{4}{Z_e}\eta_0\eta_1 H_n^{(2)\prime}(x_0)J_n'(x_1) + \frac{4}{Y_m}H_n^{(2)}(x_0)J_n(x_1)\right) = 0,
\end{cases} \tag{3}$$

where $\eta_0 = \sqrt{\varepsilon_0/\mu_0}$ ($\eta_1 = \eta_0/\sqrt{\varepsilon_r}$) is the free-space (dielectric cavity) intrinsic impedance, ω is the angular frequency, $x_0 = 2\pi r_c/\lambda_0$ and $x_1 = x_0\sqrt{\varepsilon_r}$. The prime $'$ denotes the derivative with respect to the entire argument. Assuming no losses, Z_e and Y_m are purely imaginary and take the following form:

$$Z_e^{TE} = \frac{j\eta_1 J_n'(x_1)}{2J_n(x_1)}, \qquad Y_m^{TE} = -\frac{jJ_n(x_1)}{2\eta_1 J_n'(x_1)}. \tag{4}$$

The surface electric and magnetic impedances of the cylindrical MS, required to sustain a BIC in the associated cavity, are determined from (4). This formulation depends on the cylinder's radius, the frequency and the desired order, as well as the permittivity. It is noteworthy that the condition $Z_eY_m = 1/4$ forces the field inside the cavity to zero for all modes ($B_n^{TE} = 0\,\forall n$), while the pole condition enables excitation of a specific mode. This allows single-mode BICs of any order by selecting the order n in (4) and designing a MS with the corresponding impedances. In practice, higher-order modes become increasingly sensitive to structural deviations, making them impractical. Figure S 2 (right) in the Supplementary Material shows the internal coefficients for a

quasi-BIC of order $n = 0$ in a cavity with $r_c = 0.1\lambda_0$, confirming its single-mode nature.

Solutions for the TM^z polarization can be derived by duality and are provided in the Supplementary Material. Note that the condition $Z_e = 0$ ($Y_m = 0$) corresponds to a perfect electric conductor (perfect magnetic conductor). Utilizing duality again, it is simple to show that the scenario involving the perfect magnetic conductor corresponds to the BIC conditions for the TM^z polarization in a cavity enclosed by perfect electric conductor. It is noteworthy that these specific solutions align with the cases analyzed in [31].

Considering an empty cavity, i.e $\varepsilon_r = 1$, Fig. 2 shows the normalized Z_e and Y_m curves that identify the conditions for BIC excitation as function of r_c/λ_0 for the first 4 modes. Ideally, appropriate MSs can sustain a BIC with any cylinder size, thereby enabling the possibility of BICs in sub-wavelength cavities. We observe that small cavities require extremely small or large values of Z_e and Y_m, which are challenging to achieve with physical MSs. Moreover, due to the periodic behaviour of the results, some of the other sizes also require these extreme parameters, and should therefore be avoided.

Figure 3 shows the normalized field profiles as a function of r_c/λ_0 for 4 different ideal MSs, each designed to support a quasi-BIC arising from one of the first 4 modes in a cavity of $r_c = 0.1\lambda_0$. Fields are evaluated at $(x, y) = (r_c/4, 0)$. The impedances for each BIC, derived using equations (4), correspond to the dashed-line intersections in Fig. 2. Slight detuning of these values enabled the emergence of the quasi-BICs, producing the field profiles shown in Fig. 3. Higher-order quasi-BICs show stronger but much narrower responses, indicating higher Q-factors and increased sensitivity to structural deviations.

Until now, the cylindrical MS was assumed to be infinitely thin, lossless, and homogeneous. The next step is to determine a surface design that exhibits the required impedances to excite the quasi-BIC. Periodic structures like frequency selective surfaces (FSS) and MSs can be treated as homogenized impedance sheets [31, 36–38]. Many of these surfaces have associated analytical models, but they often only include the electric response. In contrast, the spherical particle model accounts for both electric and magnetic dipoles, providing expressions for effective surface impedances for an array of spherical particles [32]. In the planar case, this model consists of an infinite grid of spherical particles with radius r_s and lattice constant d. Particles are made of a non-magnetic material with relative permittivity $\varepsilon_{r,s}$, and the grid is embedded in a non-magnetic host medium with relative permittivity $\varepsilon_{r,h}$. To ensure the dipole model holds, preventing higher-order modes from affecting the scattering mechanism, r_s must be reasonably smaller than the wavelength in the host medium, whereas d should be smaller than the wavelength to avoid diffraction. Considering the host medium to be vacuum, i.e. $\varepsilon_{r,h} = 1$, and a normal incidence of the wave on the grid, the effective

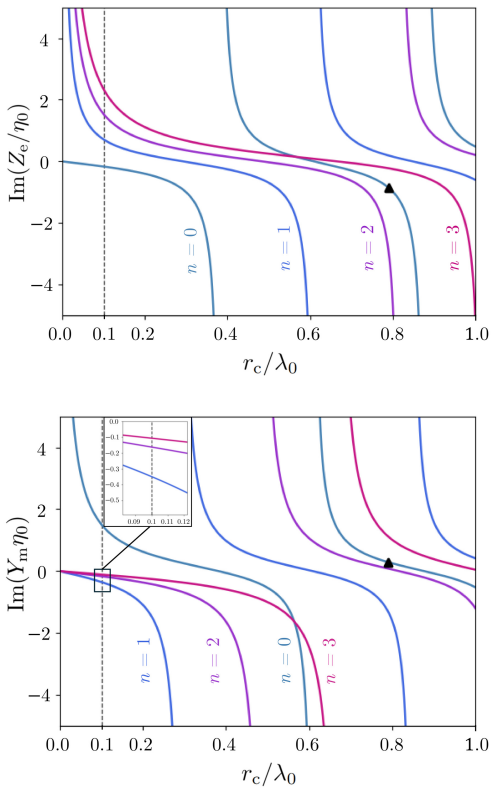

FIG. 2. Normalized imaginary part of the surface impedance (top) and admittance (bottom) curves that identify the conditions for BIC excitation for the first 4 modes as function of r_c/λ_0. The dashed line highlights BICs in a cavity with $r_c/\lambda_0 = 0.1$ whereas ▲ marks the values $(Z_e/\eta_0, Y_m\eta_0) \approx (-j0.83, j0.3)$ that identify the conditions for BIC excitation for $n = 0$ at $r_c/\lambda_0 = 0.7878$. The inset is a zoomed version of the curves that highlights the intersection with the dashed line. Note that the product Z_eY_m for the same mode n will give a constant value of 1/4.

electric impedance and magnetic admittance of the MS are described as [32]:

$$\frac{Z_e}{\eta_0} = j\left(\frac{d^2\mathrm{Re}\left(\alpha_e^{-1}\right)}{k_0} - \frac{\sin(k_0R_0)}{4} + \frac{\cos(k_0R_0)}{4k_0R_0}\right),$$
$$Y_m\eta_0 = j\left(\frac{d^2\mathrm{Re}\left(\alpha_m^{-1}\right)}{k_0} - \frac{\sin(k_0R_0)}{4} + \frac{\cos(k_0R_0)}{4k_0R_0}\right). \quad (5)$$

Here, $R_0 = d/1.438$, $\alpha_e = -j6\pi a_1/k_0^3$, and $\alpha_m = -j6\pi b_1/k_0^3$ represent the dynamic polarizabilities of a particle, where a_1 and b_1 are the dipolar Mie scattering coefficients (the definitions are provided in the Supplementary Material). Although this formulation is developed considering the planar case, it has been demonstrated to be valid for cylindrical configurations as well [31, 39–41]. In fact, impedance expressions derived for planar cases remain valid as long as particles and periods of the MS have sub-wavelength dimensions and are

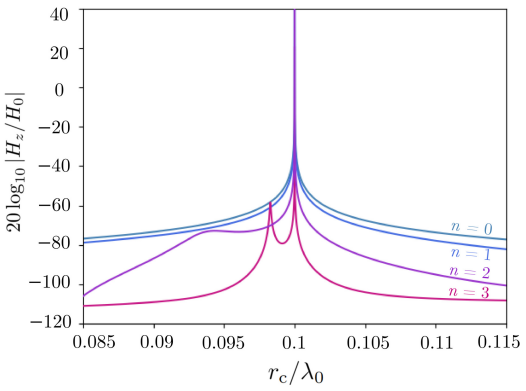

FIG. 3. Local magnetic field intensity at $(x, y) = (r_c/4, 0)$ as function of r_c/λ_0 of 4 different ideal MSs forming empty lossless cavities of radius $r_c = 0.1\lambda_0$. The MSs are designed to sustain a quasi-BIC for one of the first four modes in each respective cavity. For $n = 0, 1, 2, 3$ we have respectively $(Z_e/\eta_0, Y_m\eta_0) \approx (-j0.1654, j1.5117), (j0.7159, -j0.3492), (j1.5388, -j0.1625), (j2.3479, -j0.1065)$.

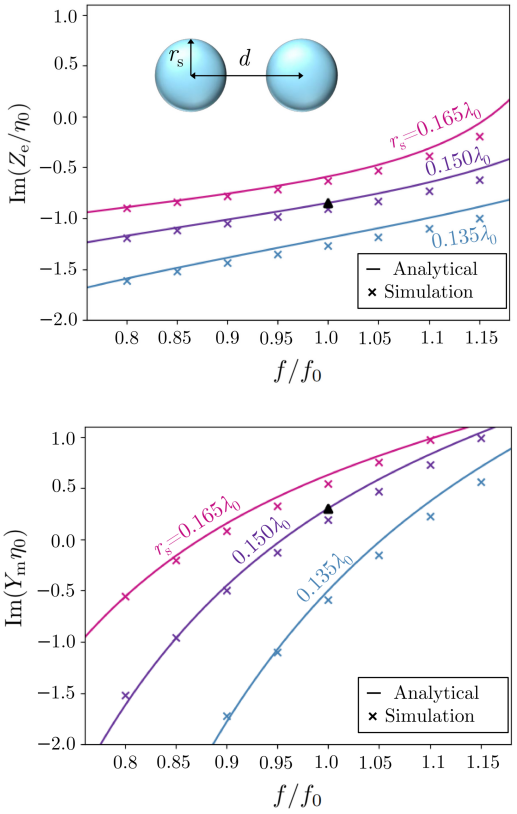

FIG. 4. Normalized imaginary part of the surface impedance (top) and admittance (bottom) of the planar MS as function of f/f_0, where f_0 is the design frequency. The analytical model corresponds to the MS description by the spherical particle model in (5), while the ticks are results from full-wave simulations. Design parameters are $\varepsilon_{r,h} = 1$, $\varepsilon_{r,s} = 12.08$ (silicon), $d = 0.45\lambda_0$ and $r_s = 0.135\lambda_0, 0.15\lambda_0, 0.165\lambda_0$. ▲ marks values $(Z_e/\eta_0, Y_m\eta_0) \approx (-j0.85, j0.3)$ obtained for $r_s = 0.15\lambda_0$ at the design frequency.

smaller than the local curvature [39]. For a more detailed discussion on angular dispersion see the Supplementary Material. To account for the finite number of particles and the cylindrical geometry, it is possible to adjust the particle radius to attain the desired values of Z_e and Y_m.

We propose a design with particles made of silicon, which at telecommunication wavelength $\lambda_0 = 1550$ nm exhibits a lossless behaviour with a relative permittivity $\varepsilon_{r,s} = 12.08$. Fig. 4 shows the surface impedance and admittance, normalized to η_0, for a planar MS with $d = 0.45\lambda_0$ and $r_s = (0.135\lambda_0, 0.15\lambda_0, 0.165\lambda_0)$ as function of frequency. Ticks identify solutions calculated from the grid transmission and reflection coefficients extracted from full-wave simulations obtained from COMSOL Multiphysics [32]. As expected, the analytical model deviates from the full-wave simulation with increasing particle size, where the surface is less homogeneous. Comparing Fig. 2 and Fig. 4, it is clear that not all of the required combinations of Z_e and Y_m can be achieved with this MS design. In general, Z_e is negative, and thus only the $n = 0$ mode can be excited for deeply sub-wavelength cavities. However, for such small cavities, there is only room for a few particles around the cylindrical interface of the cavity making the MS highly inhomogeneous. Therefore, a compromise must be made between sizes of the cavity and the dielectric particles. We select a particle radius of $r_s = 0.15\lambda_0$ with lattice constant $d = 0.45\lambda_0$, leading to a MS that, at the design frequency f_0, exhibits electric and magnetic impedances that identify the conditions for quasi-BIC excitation in a cylinder of radius $r_c = 0.7878\lambda_0$ for the $n = 0$ mode. This design is highlighted by the marker symbol ▲ in Fig. 2 and Fig. 4. A model of the cylindrical cavity with the MS design was implemented and simulated in COMSOL Multiphysics. The MS consisted of 11 particles being equidistantly distributed along the circumference of the cylinder. As already mentioned, because of the finite number of particles and the cylindrical geometry, we had to fine-tune the model to go as close as possible to the BIC condition. Eventually we found it with $r_s = 0.1542\lambda_0$ at $f \approx 0.993 f_0$. The magnetic field intensities are shown in Fig. 5, where the left figure represents the analytical ideal field given in (1) and the right figure represents the result retrieved from the full-wave simulation. There is a strong agreement of the internal fields, whereas the standing wave pattern in the simulation is disturbed due to the size of particles composing the MS contributing to the scattered field. The numerical Q-factor, defined as $Q = \mathrm{Re}\{f\}/2\mathrm{Im}\{f\}$, where f is the complex frequency obtained from the COMSOL eigenfrequency solver, is $\sim 1.7 \times 10^4$. Note that the analytical field intensity shown in Fig. 5 (left) is intended to offer a visual comparison between the analytical field pattern and the simulated one. Ideally, as the MS's impedance and admittance values approach those given by (4), the Q-factor approaches ∞, as detailed in the Supplemen-

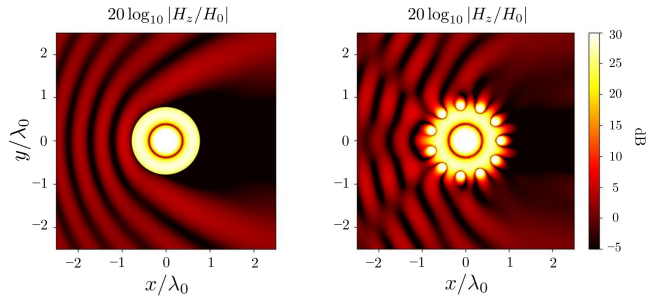

FIG. 5. Magnetic field intensity in logarithmic scale in the xy-plane. Left: analytically derived from ideal MS. Right: homogenized MS through silicon particles ($\varepsilon_{r,s} = 12.08$). Geometric parameters are $r_c = 0.7878\lambda_0$, $d = 0.45\lambda_0$ and $r_s = 0.1542\lambda_0$.

tary Material. Two more designs with smaller cavity radii ($r_c = 0.5077\lambda_0$ and $r_c = 0.2546\lambda_0$) have been investigated showing that reducing the cavity size while maintaining a quasi-BIC necessitates increasing the permittivity of the dielectric particles. The analytical and simulated magnetic field intensities can be found in the Supplementary Material. The Q-factor is lower for the smaller cavities, indicating that they are more susceptible to inhomogeneities in the MS. To make the MS more homogeneous, even smaller resonant particles are needed. Please note that an expanded discussion with additional data on how the MS homogeneity is linked to the Q-factor is provided in the Supplementary Material, along with a discussion on the practical implementation.

In this work, BICs were demonstrated in cylindrical MS cavities exhibiting effective electric and magnetic surface impedances. The analytical solutions for the required surface impedances were derived and used to show that quasi-BICs can be induced in associated cylindrical cavities of arbitrary sizes. As a proof-of-concept configuration, a MS composed of spherical silicon particles was designed using established MS homogenization models, and its ability to support the excitation of quasi-BICs was shown and further verified through full-wave analysis of the actual cylindrical MS. It should be noted that other MS designs, utilizing different materials and element shapes, can be utilized as long as they exhibit the required surface impedances [37, 38, 49]. Moreover, we expect the presence of BICs in other geometries, like planar slabs and spheres, exhibiting similar properties, although the required surface impedances will differ. Importantly, as can be seen from the boundary conditions (2), the condition $Z_e Y_m = 1/4$ (corresponding to a zero in the internal field) is general and will still apply. Despite the demonstration at optical frequencies, the proposed MS cavity design may also be of potential interest in the design of filters, antennas, sensors, and nonlinear systems at frequencies ranging from radio to mm-waves.

[1] D. C. Marinica, A. G. Borisov, and S. V. Shabanov, Bound states in the continuum in photonics, Phys. Rev. Lett. **100**, 183902 (2008).

[2] C. W. Hsu, B. Zhen, A. D. Stone, J. D. Joannopoulos, and M. Soljačić, Bound states in the continuum, Nature Reviews Materials **1**, 16048 (2016).

[3] K. Koshelev, G. Favraud, A. Bogdanov, Y. Kivshar, and A. Fratalocchi, Nonradiating photonics with resonant dielectric nanostructures, Nanophotonics **8**, 725 (2019).

[4] A. F. Sadreev, Interference traps waves in an open system: bound states in the continuum, Reports on Progress in Physics **84**, 055901 (2021).

[5] D. C. Zografopoulos and O. Tsilipakos, Recent advances in strongly resonant and gradient all-dielectric metasurfaces, Materials Advances **4**, 11 (2023).

[6] K. Koshelev, S. Lepeshov, M. Liu, A. Bogdanov, and Y. Kivshar, Asymmetric metasurfaces with high-q resonances governed by bound states in the continuum, Phys. Rev. Lett. **121**, 193903 (2018).

[7] F. Wu, X. Qi, M. Qin, M. Luo, Y. Long, J. Wu, Y. Sun, H. Jiang, T. Liu, S. Xiao, and H. Chen, Momentum mismatch driven bound states in the continuum and ellipsometric phase singularities, Phys. Rev. B **109**, 085436 (2024).

[8] A. Krasnok, D. Baranov, H. Li, M.-A. Miri, F. Monticone, and A. Alù, Anomalies in light scattering, Adv Opt Photonics **11**, 892 (2019).

[9] J. von Neumann and E. P. Wigner, Über merkwürdige diskrete eigenwerte, in *The Collected Works of Eugene Paul Wigner: Part A: The Scientific Papers*, edited by A. S. Wightman (Springer Berlin Heidelberg, Berlin, Heidelberg, 1993) pp. 291–293.

[10] M. Amrani, I. Quotane, C. Ghouila-Houri, E. H. El Boudouti, L. Krutyansky, B. Piwakowski, P. Pernod, A. Talbi, and B. Djafari-Rouhani, Experimental evidence of the existence of bound states in the continuum and fano resonances in solid-liquid layered media, Phys. Rev. Appl. **15**, 054046 (2021).

[11] F. Ursell, Trapping modes in the theory of surface waves, Mathematical Proceedings of the Cambridge Philosophical Society **47**, 347–358 (1951).

[12] M. Kang, T. Liu, C. T. Chan, *et al.*, Applications of bound states in the continuum in photonics, Nature Reviews Physics **5**, 659 (2023).

[13] F. Monticone, H. M. Doeleman, W. den Hollander, A. F. Koenderink, and A. Alù, Trapping light in plain sight: Embedded photonic eigenstates in zero-index metamaterials, Laser & Photonics Reviews **12** (2018).

[14] F. Monticone and A. Alù, Embedded photonic eigenvalues in 3d nanostructures, Physical Review Letters **112**, 213903 (2014).

[15] S. I. Azzam, V. M. Shalaev, A. Boltasseva, and A. V. Kildishev, Formation of bound states in the continuum in hybrid plasmonic-photonic systems, Phys. Rev. Lett. **121**, 253901 (2018).

[16] R. E. Jacobsen, A. Krasnok, S. Arslanagić, A. V. Lavrinenko, and A. Alú, Boundary-induced embedded eigenstate in a single resonator for advanced sensing, ACS

Photonics **9**, 1936 (2022).
[17] C. Zhou, L. Huang, R. Jin, L. Xu, G. Li, M. Rahmani, X. Chen, W. Lu, and A. E. Miroshnichenko, Bound states in the continuum in asymmetric dielectric metasurfaces, Laser & Photonics Reviews **17** (2022).
[18] Z. Jing, J. Wang, L. Gao, and W. Qiu, High-sensitivity sensing in all-dielectric metasurface driven by quasi-bound states in the continuum, Nanomaterials **13** (2023).
[19] Z. Chen, X. Yin, J. Jin, Z. Zheng, Z. Zhang, F. Wang, L. He, B. Zhen, and C. Peng, Observation of miniaturized bound states in the continuum with ultra-high quality factors, Science Bulletin **67**, 359 (2022).
[20] Z. Wang, Y. Liang, J. Qu, M. K. Chen, M. Cui, Z. Cheng, J. Zhang, J. Yao, S. Chen, and D. P. Tsai, Plasmonic bound states in the continuum for unpolarized weak spatially coherent light, Photonics Res. **11**, 260 (2023).
[21] Y. Liang, K. Koshelev, F. Zhang, H. Lin, S. Lin, J. Wu, B. Jia, and Y. Kivshar, Bound states in the continuum in anisotropic plasmonic metasurfaces, Nano Letters **20**, 6351 (2020).
[22] Y. Liang, H. Lin, S. Lin, J. Wu, W. Li, F. Meng, Y. Yang, X. Huang, B. Jia, and Y. Kivshar, Hybrid anisotropic plasmonic metasurfaces with multiple resonances of focused light beams, Nano Letters **21**, 8917 (2021).
[23] A. Aigner, A. Tittl, J. Wang, T. Weber, Y. Kivshar, S. A. Maier, and H. Ren, Plasmonic bound states in the continuum to tailor light-matter coupling, Science Advances **8**, eadd4816 (2022).
[24] Y. Liang, D. P. Tsai, and Y. Kivshar, From local to nonlocal high-q plasmonic metasurfaces, Phys. Rev. Lett. **133**, 053801 (2024).
[25] K. Koshelev, S. S. Kruk, E. V. Melik-Gaykazyan, J.-H. Choi, A. A. Bogdanov, H.-G. Park, and Y. S. Kivshar, Subwavelength dielectric resonators for nonlinear nanophotonics, Science **367**, 288 (2019).
[26] M. V. Rybin, K. Koshelev, Z. Sadrieva, K. Samusev, A. A. Bogdanov, M. Limonov, and Y. S. Kivshar, High-q supercavity modes in subwavelength dielectric resonators, Physical Review Letters **119**, 243901 (2017).
[27] M. Odit, K. Koshelev, S. Gladyshev, K. Ladutenko, Y. Kivshar, and A. Bogdanov, Observation of supercavity modes in subwavelength dielectric resonators, Advanced Materials **33**, 2003804 (2021).
[28] R. E. Jacobsen and S. Arslanagić, Supercavity mode in a single metallic resonator, Applied Physics Letters **123**, 221701 (2023).
[29] A. Krasnok and A. Alú, Embedded scattering eigenstates using resonant metasurfaces, Journal of Optics **20**, 064002 (2018).
[30] F. S. Cuesta, V. S. Asadchy, A. D. Sayanskiy, V. A. Lenets, M. S. Mirmoosa, X. Ma, S. B. Glybovski, and S. A. Tretyakov, Nonscattering metasurface-bound cavities for field localization, enhancement, and suppression, IEEE Transactions on Antennas and Propagation **68**, 1689 (2020).
[31] R. E. Jacobsen and S. Arslanagić, Extreme localization of fields in open cylindrical impedance surface cavities, IEEE Transactions on Antennas and Propagation **72**, 1686 (2024).
[32] A. Monti, A. Alù, A. Toscano, and F. Bilotti, Surface impedance modeling of all-dielectric metasurfaces, IEEE Transactions on Antennas and Propagation **68**, 1799 (2020).
[33] C. F. Bohren and D. R. Huffman, *Absorption and Scattering of Light by Small Particles*, 1st ed. (Wiley, New York, NY, USA, 1983).
[34] S. A. Tretyakov, Metasurfaces for general transformations of electromagnetic fields, Philosophical Transactions of the Royal Society A: Mathematical, Physical and Engineering Sciences **373**, 20140362 (2015).
[35] C. Pfeiffer and A. Grbic, Bianisotropic metasurfaces for optimal polarization control: Analysis and synthesis, Phys. Rev. Appl. **2**, 044011 (2014).
[36] S. Tretyakov, *Analytical Modeling in Applied Electromagnetics* (Artech House, 2003).
[37] O. Luukkonen, C. Simovski, G. Granet, G. Goussetis, D. Lioubtchenko, A. V. Räisänen, and S. A. Tretyakov, Simple and accurate analytical model of planar grids and high-impedance surfaces comprising metal strips or patches, IEEE Trans Antennas Propag **56**, 1624 (2008).
[38] H. Xiong, M. C. Tang, Y. H. Peng, Y. H. Zhong, and X. H. Tan, Surface impedance of metasurfaces/graphene hybrid structures, Nanoscale Res Lett **14**, 1 (2019).
[39] Y. R. Padooru, A. B. Yakovlev, P.-Y. Chen, and A. Alù, Analytical modeling of conformal mantle cloaks for cylindrical objects using sub-wavelength printed and slotted arrays, Journal of Applied Physics **112**, 034907 (2012).
[40] A. Monti, A. Alù, A. Toscano, and F. Bilotti, Optical invisibility through metasurfaces made of plasmonic nanoparticles, J Appl Phys **117**, 123103 (2015).
[41] R. E. Jacobsen, A. V. Lavrinenko, and S. Arslanagić, Reconfigurable dielectric resonators with imbedded impedance surfaces - from enhanced and directional to suppressed scattering, Applied Physics Letters **122**, 81701 (2023).
[42] W. Liu, Z. Li, H. Cheng, and S. Chen, Dielectric resonance-based optical metasurfaces: From fundamentals to applications, iScience **23**, 101868 (2020).
[43] W. Yang, J. Zhou, D. P. Tsai, and S. Xiao, Advanced manufacturing of dielectric meta-devices, Photonics Insights **3**, R04 (2024).
[44] J. Proust, F. Bedu, S. Chenot, I. Soumahoro, I. Ozerov, B. Gallas, R. Abdeddaim, and N. Bonod, Chemical alkaline etching of silicon mie particles, Advanced Optical Materials **3**, 1280 (2015).
[45] U. Zywietz, A. B. Evlyukhin, C. Reinhardt, and B. N. Chichkov, Laser printing of silicon nanoparticles with resonant optical electric and magnetic responses, Nature Communications **5**, 3402 (2014).
[46] Y. Lisunova, M. Spieser, R. Juttin, F. Holzner, and J. Brugger, High-aspect ratio nanopatterning via combined thermal scanning probe lithography and dry etching, Microelectronic Engineering **180**, 20 (2017).
[47] Y. Wang, Q. Chen, W. Yang, Z. Ji, L. Jin, X. Ma, Q. Song, A. Boltasseva, J. Han, V. M. Shalaev, and S. Xiao, High-efficiency broadband achromatic metalens for near-ir biological imaging window, Nature Communications **12**, 5560 (2021).
[48] V. J. Einck, M. Torfeh, A. McClung, D. E. Jung, M. Mansouree, A. Arbabi, and J. J. Watkins, Scalable nanoimprint lithography process for manufacturing visible metasurfaces composed of high aspect ratio tio2 meta-atoms, ACS Photonics **8**, 2400 (2021).
[49] H. Younesiraad, Z. Hamzavi-Zarghani, and L. Matekovits, Invisibility utilizing huygens' metasurface based on mantle cloak and scattering suppression phenomen, IEEE Trans Antennas Propag **69**, 5181 (2021).